Int. J. Solids Structures Vol. 31, No. 1, pp. 1–26, 1994
Printed in Great Britain

0020–7683/94 $6.00+ .00

NEAR-TIP FIELD CHARACTERIZATION AND *J*-INTEGRAL EVALUATION FOR NONPROPORTIONAL LOADS

JONAS FALESKOG and PER NORDLUND
Department of Solid Mechanics, Royal Institute of Technology, Stockholm, Sweden

(*Received* 11 *March* 1993; *in revised form* 7 *July* 1993)

Abstract—The *J*-integral is calculated numerically using the domain integral method and a contour integral according to the definition of the *J*. It was conjectured that the methods could give conflicting results for nonproportional loads. It is found, however, that both methods give satisfactory results conforming even for highly nonproportional loads. In plane strain, the near-tip field could successfully be characterized by a two-parameter description according to the *J*-*Q* theory. Remotely applied nonproportional loads corresponded to different paths in the *J*-*Q* space. This was demonstrated in the range of small-scale yielding up to fully yielded situations.

1. INTRODUCTION

Among the central problems in fracture mechanics analysis is the evaluation of the *J*-integral. Even more important is whether *J* can characterize the crack front state. Originally *J* was defined (Rice, 1968; Eshelby, 1970) for purely elastic conditions as a contour integral (correspondingly a surface integral in three dimensions, cf. Budiansky and Rice, 1973). Computational considerations motivated a development of area integration (or volume integration in three dimensions) by the so-called virtual crack extension method (Parks, 1974) or domain integral method (Li *et al.*, 1986; Shih *et al.*, 1986; Nakamura *et al.*, 1985). These methods can easily be shown to be mathematically equivalent to the contour integration for an elastic problem free of volume forces and thermal gradients. As the *J*-integral concept has been extended to incremental elasto–plastic problems this equivalence ceases to be a strict mathematical fact. For cases of nearly proportional loading, or more precisely for cases when the contour integral is nearly path independent, the equivalence still holds in an approximate sense. For strongly nonproportional loads, differences between the two formulations may occur. In many engineering problems the external loading is nonproportional, for instance when mechanical and thermal loads interact. Another case when the stress state in the crack front vicinity is strongly nonproportional is when the crack starts to grow. It can be shown that for conventional incremental plasticity laws the strain singularity at a quasi-statically growing tip is so weak (for the plane small strain case: cf. Slepyan, 1974, for perfect elasto-plasticity and Amazigo and Hutchinson, 1977, for linearly hardening materials) that the near tip value of the contour definition of *J* approaches zero as the integration path is shrunk towards zero. In this case one obviously has to rely on far-field values of the *J*-integral. It is then a question of whether some unambiguous value can really be obtained from a FEM calculation.

In the present study, the fact that the different computational methods may lead to different results is examined. Results obtained with the commercial finite element code ABAQUS (1989), which uses the domain integral method, are compared with results computed through contour integration in accordance with the original definition of the *J*-integral.

In the case of proportional loading investigators like McMeeking and Parks (1979), Shih and German (1981) and Betegon and Hancock (1991) have examined under which conditions *J* alone characterizes the crack tip state. It was found that *J*-dominance prevails at large loads only in rather deeply cracked specimens. In some geometries the loading has to be so low for *J*-dominance that even linear elastic fracture mechanics should apply. To cope with these problems a two parameter description is motivated. Recently O'Dowd and Shih (1991, 1992), Du and Hancock (1991) and Betegon and Hancock (1991) have suggested

such descriptions. These models are the same if small scale yielding conditions are satisfied. In the case of remotely applied nonproportional loads, Sönnerlind and Kaiser (1986) investigated if a remote path independent J-value can be reached. By investigating a SEN specimen they established that this could be found. In the present study the question of whether the J-integral characterizes the crack tip state under remotely applied nonproportional loads, provided a path independent value of J is found, is investigated for the plane strain case. The near-tip fields are then characterized by adopting the J-Q theory (cf. O'Dowd and Shih, 1991, 1992), since this two-parameter description is more suited to fully yielded situations. In this two-parameter description, Q only is expected to parameterize the stress and strain distributions when distances are normalized by J/σ_Y. Here σ_Y is the yield stress.

The studied examples involve combined bending and tension in two and three dimensions and simulated crack growth in three dimensions. Large deformations are taken into account throughout the analysis, except in some linearly elastic test examples and one two-dimensional example where a small-strain approximation was utilized for comparison reasons. This was chosen in order to get a more complete solution of the plastic deformation close to the crack front for the purpose of investigating the near-tip fields.

2. J-INTEGRAL FORMULATIONS

2.1. *Line integral definition*

The J-integral for the two-dimensional case, without body forces and tractions on the crack surfaces, taking large deformations into account, is defined by (cf. Eshelby, 1970):

$$J = \int_\Gamma \left(W\delta_{1j} - P_{ji}\frac{\partial u_i}{\partial X_1}\right) n_j \, \mathrm{d}\Gamma, \tag{1}$$

with the deformation work per unit volume defined by:

$$W = \int_0^{\partial u_i/\partial X_j} P_{ji} \, \mathrm{d}\left(\frac{\partial u_i}{\partial X_j}\right). \tag{2}$$

The stress measure used is the first Piola–Kirchhoff stress given as:

$$P_{ij} = |F|\sigma_{pj}\frac{\partial X_i}{\partial x_p}. \tag{3}$$

Here σ_{ij} is the Cauchy stress, $|F|$ the ratio of volume in the current configuration to volume in the undeformed configuration, u_i the displacement and X_i the position of a material point in the undeformed configuration and thus $x_i = X_i + u_i$. Γ is a curve in the undeformed configuration embracing the crack tip, beginning on the lower crack surface and ending on the upper one and $\mathbf{n}$ the normal vector, pointing outward from the curve Γ. The definition of W can also be expressed as:

$$W = \int_0^{t_d} |F|\sigma_{ij}D_{ij} \, \mathrm{d}t, \tag{4}$$

where t is a loading parameter which is zero in the undeformed state and equal to t_d in the deformed state for which W is to be computed. The rate of deformation tensor D_{ij} is defined as the symmetric part of the spatial velocity gradient. In ABAQUS the deformation work is calculated using the form according to eqn (4).

In three dimensions the J-value related to a point s on the crack front can be formally defined (cf. Bakker, 1984; Carpenter *et al.*, 1986) by the expression (5). The coordinate system is assumed to be oriented so that the X_1-axis lies in the crack plane and is a normal

to the crack front at the considered point. The X_3-axis is tangential to the crack front and the X_2-axis is perpendicular to the crack plane:

$$J(s) = \int_\Gamma \left(W\delta_{1j} - P_{ji}\frac{\partial u_i}{\partial X_1} \right) n_j \, \mathrm{d}\Gamma - \int_{A_\Gamma} \frac{\partial}{\partial X_3}\left(P_{3i}\frac{\partial u_i}{\partial X_1} \right) \mathrm{d}A. \tag{5}$$

Here Γ is a curve in the undeformed configuration enclosing the crack front, at a position given by s, in the plane $X_3 = 0$. The normal vector pointing outward from the curve Γ is denoted by $\mathbf{n}$ and A_Γ is the surface area defined by Γ as depicted in Fig. 1(a).

2.2. *The domain integration method*

The J-evaluation method of ABAQUS (1989) is based on the domain integration technique developed by Shih *et al.* (1986). The crucial point in their derivation of the final expression of J is the existence of a strain energy density function. The domain integral expressions for J below will be denoted G to emphasize the difference with the eqns (1)–(5). Also in the expressions below, thermal strain, body forces and crack surface tractions are assumed to be absent.

In two dimensions the domain integral expression is:

$$G = \int_A \left(P_{ji}\frac{\partial u_i}{\partial X_1} - W\delta_{1j} \right) \frac{\partial q_1}{\partial X_j} \, \mathrm{d}A. \tag{6}$$

Here A is the area depicted in Fig. 1(b) and q_1 is a sufficiently smooth function in the region A chosen to be unity on Γ and zero on C, where the contour C can be seen in Fig. 1(b). Equation (6) can now by use of the divergence theorem, the equations of equilibrium, $\partial P_{ji}/\partial X_j = 0$, and the properties of q_1, be written as:

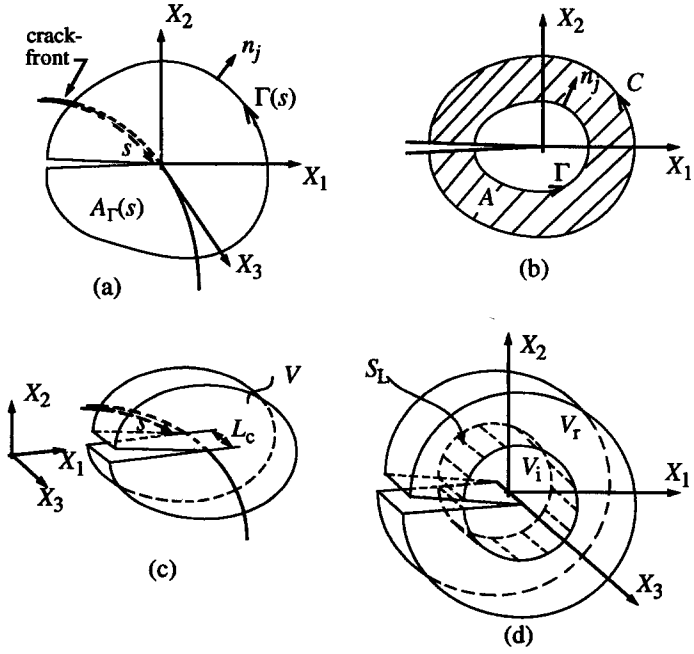

Fig. 1. (a) Definition of local orthogonal Cartesian coordinate system at the point S on the crack front. (b) Definition of the integration domain for the domain integral (two dimensions). (c) Definition of the integration domain for the domain integral (three dimensions). (d) The volume V, in (c), is divided into subvolumes V_r and V_i, which are separated by the surface S_L.

$$G = \int_\Gamma \left(W\delta_{1j} - P_{ji}\frac{\partial u_i}{\partial X_1} \right) n_j \, \mathrm{d}\Gamma - \int_A \left(P_{ji}\frac{\partial^2 u_i}{\partial X_j \partial X_1} - \frac{\partial W}{\partial X_1} \right) q_1 \, \mathrm{d}A. \tag{7}$$

By comparing eqns (1) and (7) the remaining area integral in eqn (7) thus expresses the difference between the contour integral and the domain integral. In general it vanishes only if the material is (possibly nonlinearly) elastic or if the stressing is purely proportional. This fact has of course been well-known for a long time (for a discussion cf. Moran and Shih, 1987; Nilsson and Ståhle, 1988) but it seems that it has not always been appreciated. It should be mentioned that for incremental plasticity with nonproportional loading, neither eqn (1) nor eqn (6) can be interpreted as the energy release rate and path independence may not be expected. However, if a path independent J-value can be found, it could still serve as crack-tip state characterizing parameter.

In the development of a local value of J in three dimensions, Shih *et al.* (1986) derived:

$$G_A = \int_V \left(P_{ji}\frac{\partial u_i}{\partial X_k} - W\delta_{kj} \right) \frac{\partial \mathbf{q}_k}{\partial X_j} \, \mathrm{d}V. \tag{8}$$

Here G_A could be interpreted as a weighted J-value along a segment of the crack front, L_c, where the crack plane is oriented in the X_1–X_3 plane and V is the volume embracing L_c, see Fig. 1(c). If the material is elastic, $G_A = \delta U/\delta a$ is the energy release rate extending the crack $q_k \delta a$ along the crack front segment L_c. Here U is the potential energy, a is the crack length and the direction of q_k is normal to the crack front in the X_1–X_3 plane. While discussing the vector field q_k it is fruitful to divide the volume V into subvolumes V_r and V_i, in analogy to the two-dimensional case, as depicted in Fig. 1(d). In the figure, S_L is the surface separating the volumes V_r and V_i. The vector field q_k is zero on the outer boundary to V, excluding the crack faces and the crack front, and has a finite value on the surface S_L [Fig. 1(d)]. In V_i, q_k depends on X_1 and X_3 only and in V_r, q_k is an arbitrary sufficiently smooth function. With the chosen coordinate system, q_2 is zero in V. For simplicity and without loss of generality, let the segment L_c of the crack front be straight, with the coordinate system defined as before. Then q_k will reduce to q_1 and in V_i, q_1 is a function of X_3 only. With use of the divergence theorem, the equations of equilibrium and the properties of q_1, eqn (8) can be written as:

$$G_A = \int_{S_L} \left(W\delta_{1j} - P_{ji}\frac{\partial u_i}{\partial X_1} \right) n_j q_1 \, \mathrm{d}S - \int_{V_r} \left(P_{ji}\frac{\partial^2 u_i}{\partial X_j \partial X_1} - \frac{\partial W}{\partial X_1} \right) q_1 \, \mathrm{d}V + \int_{V_i} P_{3i}\frac{\partial u_i}{\partial X_1}\frac{\partial q_1}{\partial X_3} \, \mathrm{d}V. \tag{9}$$

Note that S_L is the only part of the surface surrounding V_r where q_1 is different from zero.

In order to find a comparative J-value from the contour integral, eqn (5), a weighted value, J_A, over the straight crack front segment L_c, can be expressed as:

$$J_A = \int_{L_c} q_1(X_3) J(X_3) \, \mathrm{d}X_3 = \int_{S_L} \left(W\delta_{1j} - P_{ji}\frac{\partial u_i}{\partial X_1} \right) n_j q_1 \, \mathrm{d}S - \int_{V_i} \frac{\partial}{\partial X_3}\left(P_{3i}\frac{\partial u_i}{\partial X_1} \right) q_1 \, \mathrm{d}V, \tag{10}$$

where $J(X_3)$ is given by eqn (5), noting that s could be interchanged for X_3 for this particular case, and q_1 is now interpreted as a weight function depending on X_3 only.

The difference between the domain integral, eqn (9), and the contour integral, eqn (10), is obtained as:

$$G_A - J_A = -\int_{V_r} \left(P_{ji} \frac{\partial^2 u_i}{\partial X_j \partial X_1} - \frac{\partial W}{\partial X_1} \right) q_1 \, dV. \tag{11}$$

The conclusion for the difference is the same as in the two-dimensional situation discussed above.

If the contour Γ in eqn (7) [implicit in eqn (6)] and the volume V_i in eqn (9) [implicit in eqn (8)] is shrunk to zero the vector function q_1 can be referred to as a "pyramid" function. In the other case when Γ and V_i remain finite, q_1 can be referred to as a "plateau" function. Computational aspects have motivated the use of a plateau function, since in general, the numerical resolution of the near-tip fields is less accurate than the numerical resolution of the remote fields, as discussed by Shih *et al.* (1986).

In ABAQUS a plateau function is chosen for both two- and three-dimensional cases. The ring of elements through which the current integration path passes will in the two-dimensional case correspond to the area A in eqn (6) [see also Fig. 1(a)] and will in the three-dimensional case correspond to the volume V_r in eqn (9) [see Fig. 1(d)], but for this case elements situated inside, in volume V_i, will also contribute to the final J-value. The radial distance, in undeformed configuration, from the crack tip to A and to V_r, respectively will be referred to as the contour radius (R_{contour}) below.

2.3. *Implementation of the contour integral method*

In order to perform J-integral evaluations according to the contour integral method a post-processor to ABAQUS was developed. In two dimensions, corresponding to eqn (1), the integration path is chosen as a line through the Gauss points of the elements. Geometry, displacements, stresses and deformation work from ABAQUS are used to evaluate the value of the integrand.

In the three-dimensional case, eqn (10) is employed, where a local coordinate system, oriented as shown in Fig. 1(a), is fixed to the midpoint of the crack front segment L_c. Furthermore, if the function q_1 is chosen as unity, an average J-value ($\bar{J}$) per unit crack advance in the local X_1-direction can be defined as:

$$\bar{J} = \frac{1}{L_c} \int_{A_i} \left(W \delta_{1j} - P_{ji} \frac{\partial u_i}{\partial X_1} \right) n_j \, dA. \tag{12}$$

Here A_i is the surface in undeformed configuration surrounding the volume V_i and n_j is the normal, pointing outward from the surface element dA. The contour integral representation (12) is comparable to the expression used by Bakker (1984), where both the integration methods were compared under proportional loading. The meshes used here have a region of elements that follows the possibly curved crack front. This region is divided into slices of one element thickness. The J-integral is evaluated for each of these slices to give average local values of J along the crack front passing through the crack tip element, as described above. The surface (for each slice) to be integrated over is divided into three parts: One top part through the Gauss points, corresponding to the path in two dimensions, and two side parts, being the two opposite sides of the elements in V_i. Since the two side parts do not pass through the Gauss points interpolation is needed. In the case of an isoparametric 20-noded solid brick element with reduced integration a trilinear interpolation is used. In the expression for the J-integral, eqn (12), L_c is the projected length of the appropriate crack front element on the local X_3-axis in the undeformed configuration.

In order to make a fair comparison with the domain integral method, an average J-value over one slice is calculated for this method as well. In ABAQUS, as well in Shih *et al.* (1986), $J(s)$ is interpolated using the same order of interpolation as used in the elements abutting the crack front, i.e.:

$$J(s) = \sum_{I=1}^{N} J_I \Psi_I(s), \tag{13}$$

where $\Psi_I(s)$ are the piecewise quadratic shape functions in the present model. The value of

$J(s)$ at the Ith node on the crack front is denoted J_I and N is the total number of nodes along the crack front. Using eqn (13) the average domain integral value over one element, henceforth called $\bar{G}$, is given by:

$$\bar{G} = (J_{I-1} + 4J_I + J_{I+1})/6, \tag{14}$$

where I refers to the midpoint node of the crack front element in question. $\bar{G}$ is then computed for each contour in all element slices along the crack front.

3. PROBLEMS STUDIED AND FEM MODELLING

Three example problems are studied: combined bending and tension in two and three dimensions and simulated crack growth in three dimensions. The result for the particular problem will follow immediately after each problem statement.

In the code of the general purpose finite element program, ABAQUS, an updated Lagrangian formulation is used. The algorithm of Hughes and Winget (1980) is employed to account for rigid body rotations during large elastic–plastic deformation. The governing equations are then given on rate form. The material under consideration is assumed to be homogeneous, elastic–plastic with isotropic hardening and to obey the von Mises yield criterion and its associated flow rule. The constitutive law, discussed by McMeeking and Rice (1975), accounts for possible rotations of principal axes and can be expressed as:

$$\overset{\nabla}{\tau}_{ij} = 2G\left(\delta_{ik}\delta_{jl} + \frac{\nu}{1-2\nu}\delta_{kl}\delta_{ij} - \frac{1}{\dfrac{h}{3G}+1}\frac{3\tau'_{ij}\tau'_{kl}}{2\bar{\tau}^2}\right)D_{kl}, \tag{15}$$

for plastic loading and

$$\overset{\nabla}{\tau}_{ij} = 2G\left[\delta_{ik}\delta_{jl} + \frac{\nu}{1-2\nu}\delta_{kl}\delta_{ij}\right]D_{kl} \tag{16}$$

for elastic loading or any unloading. Here τ_{ij} is the Kirchhoff stress tensor defined by

$$\tau_{ij} = |F|\sigma_{ij}. \tag{17}$$

Poisson's ratio is denoted by ν, the shear modulus by G, δ_{ij} is the Kronecker delta,

$$\tau'_{ij} = \tau_{ij} - \tfrac{1}{3}\delta_{ij}\tau_{kk}, \quad \bar{\tau}^2 = \tfrac{3}{2}\tau'_{ij}\tau'_{ij}, \tag{18}$$

h is the slope of the uniaxial Kirchhoff stress vs logarithmic plastic strain curve and the symbol ∇ denotes the co-rotational stress-rate. In all examples below, the uniaxial response of the material is approximated by a piecewise linear function in the FEM model. All constitutive parameters are given in relation to Cauchy stresses, since this is required as input to ABAQUS, and then transferred to correspond toKirchhoff stresses within ABAQUS. The output from ABAQUS is also Cauchy stresses. In all examples below, the relative difference between the Kirchhoff and Cauchy stresses is of the order of stress divided by elastic modulus and thus very small. The governing equations of equilibrium, including the effects of volume change and finite strains, are enforced through a variational procedure similar to that discussed by McMeeking and Rice (1975).

In the finite element models, biquadratic eight-noded isoparametric plane strain elements are used for the two-dimensional cases and triquadratic 20-noded solid brick elements for the three-dimensional cases. In both the two-dimensional and three-dimensional cases, elements with reduced integration are used, except in the elements close to the crack tip (crack front) where elements with full integration are used. This choice is made

in order to prevent hourglassing, especially for elements with a free surface. Since a state of near incompressibility prevails close to the crack tip in the two-dimensional cases, mesh locking can occur in fully integrated elements. To circumvent this effect a selective reduced integration technique (Nagtegaal *et al.*, 1977) is used.

The crack tip is not modelled as being initially sharp in the elastic–plastic cases. Instead a small notch is used, see Fig. 2(c). The element distortions are more easily controlled with this type of mesh. For the load levels of interest in the present context, the crack-tip opening displacement is much larger than the initial notch radius. Therefore, the influence of the notch on the fields is insignificant (cf. McMeeking, 1977a; Moran *et al.*, 1990). In some examples in combined bending and tension a linear elastic material is used. In these examples the nodes at the crack tip are tied together and the midnodes along the radial edges are placed at the appropriate quarter positions so that the displacement gradient contains terms that are of order $1/(\sqrt{r})$ (cf. Barsoum, 1977), which is consistent with crack-tip fields for linearly elastic bodies (Fig. 2(d)).

The load levels are measured by a nondimensional parameter λ, defined by:

$$\lambda = \frac{J}{L\sigma_Y}, \tag{19}$$

where L is a characteristic length in the problem and σ_Y is the yield stress. Note that λ also describes the ratio between the size of near-tip field, which is of the order of J/σ_Y, and the characteristic length. The ASTM condition for linear fracture mechanics to be applicable is that λ should be smaller than about 1/1400 for the two-dimensional analysis and 1/2200 for the three-dimensional analysis. The difference is due to different E/σ_Y in the respective cases, where E denotes Young's modulus. For deep cracks, the corresponding condition

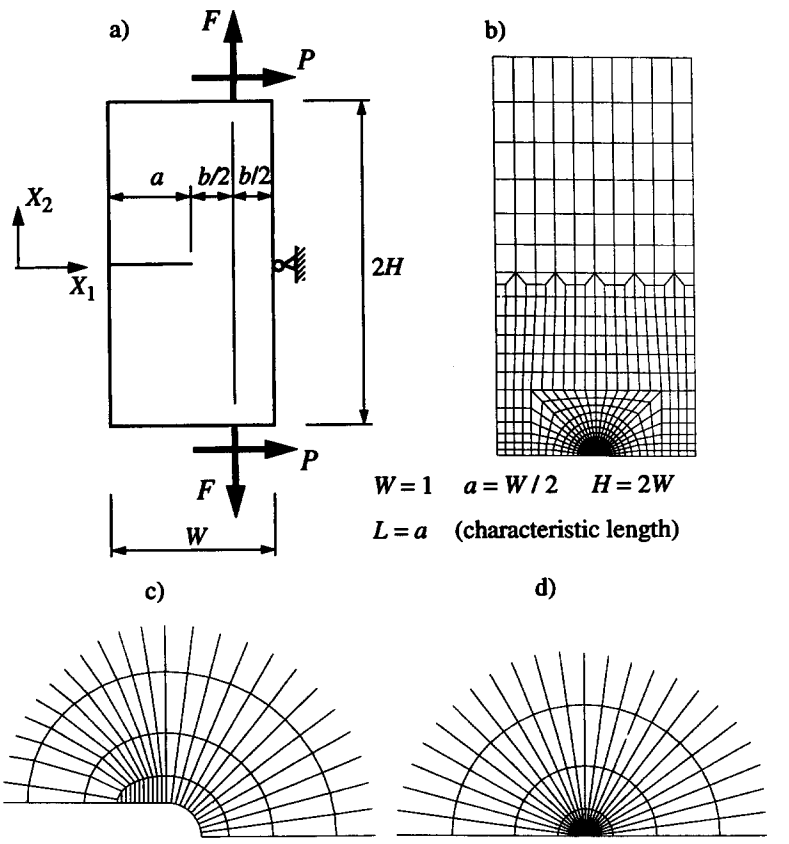

Fig. 2. The two-dimensional example investigated—SEN specimen: (a) geometry and boundary conditions, (b) finite element mesh, (c) crack-tip model for nonlinear analysis and (d) crack-tip model for linear analysis.

Table 1. λ-values and applied normalized forces at the different load levels. The l-value for the final load is based on the proportional loading sequence

Load level	1	2	3	4
λ_0	1/8000	1/1200	1/400	1/200
λ	$\approx$1/1896	$\approx$1/143	$\approx$1/28.8	$\approx$1/12.1
$\tilde{F}$	0.424	1.01	1.11	1.17
$\tilde{P}$	0.193	0.49	0.82	1.05

for J-dominated nonlinear fracture mechanics is $\lambda < 1/25$ for bending and $\lambda < 1/200$ for tension (cf. McMeeking and Parks, 1979; Shih and German, 1981).

3.1. *Example 1: combined bending and tension in two dimensions*

First a nonproportional loading situation in two dimensions is considered. A single edge cracked specimen (SEN) under plane strain conditions is chosen since it is easy to apply the extremes of tension and bending. The geometry and the finite element mesh are shown in Fig. 2. For symmetry reasons only the upper half of the body is modelled. The top and bottom edges of the model are constrained to remain straight, but contraction is allowed in the X_1-direction. Since the deformation of the initial notch becomes extremely large, the size of the initial notch radius, ρ_0, is increased in problems with larger load levels. It will, however, always remain small compared to the crack length, a, and to the blunted crack tip. The chosen initial notch radius, ρ_0, are $0.2\times10^{-4}a$, $0.5\times10^{-4}a$, $6.0\times10^{-4}a$ and $6.0\times10^{-4}a$ for the load levels 1, 2, 3 and 4, respectively. The number of elements in the circular region in the separate models are 839, 839, 671 and 671 for the load levels 1, 2, 3 and 4, respectively, and in all models there are 238 elements in the remaining part.

The loads are applied in three ways: tension followed by bending, bending followed by tension and both applied simultaneously at proportional loading. This is repeated for four different load levels which are chosen so that each of F and P alone would give the same λ-values, called λ_0, which are shown in Table 1. Here also the λ-values, based on the proportional loading case, for the final load levels are given. In the expression of λ, eqn (19), L is equal to the crack length, a. The applied forces are normalized by their respective limit loads, i.e.

$$\tilde{F} = F/F_L, \quad \tilde{P} = P/P_L, \tag{20}$$

where

$$F_L = \frac{2}{\sqrt{3}}\sigma_Y(W-a)t \quad \text{and} \quad P_L = 1.45\sigma_Y(W-a)^2\frac{t}{4H}. \tag{21}$$

The limit loads, eqn (21), correspond to solutions summarized by McClintock (1971) and agree well with the overall behaviour of the force vs displacement curves for the pure tension and the pure bending case, respectively. Following Rice (1972), a generalized combined tension–bending yield surface is derived as depicted in Fig. 3 together with the different loading sequences.

3.1.1. *Results: combined bending and tension in two dimensions.* To check the implemented contour integral routine, corresponding to eqn (1), a problem with a linear elastic material ($\nu = 0.3$), is studied. The mean J-value together with the maximum variation can be seen in Table 2. The mean value is calculated using J-values from contours passing through the 4th to the 35th element ring surrounding the crack tip, with $R_4 \approx 3\times10^{-4}a$ and $R_{35} \approx 0.65a$ (the radial distances from the crack tip to the respective contour). The result using the contour integral method agrees very well with the result using the domain-integral method (ABAQUS), although the former method shows a somewhat greater scatter around the mean J-value.

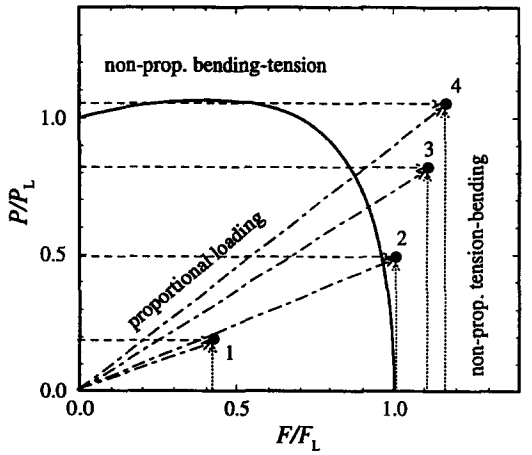

Fig. 3. Loading sequences for the SEN specimen and generalized combined tension–bending yield surface according to Rice (1972).

The elastic–plastic finite strain analysis is carried out for a material with $\nu = 0.3$, $\varepsilon_Y = \sigma_Y/E = 1/500$ and the hardening properties in eqn (15) are described by a power law hardening material with $n = 10$ in a uniaxial stress-strain law of the form:

$$\left(\frac{\bar{\sigma}}{\sigma_Y}\right)^n = \frac{\bar{\sigma}}{\sigma_Y} + \frac{\bar{\varepsilon}^p}{\varepsilon_Y}, \tag{22}$$

where the effective Cauchy stress

$$\bar{\sigma} = (\tfrac{3}{2}\sigma'_{ij}\sigma'_{ij})^{1/2}, \quad \sigma'_{ij} = \sigma_{ij} - \tfrac{1}{3}\sigma_{kk}, \tag{23}$$

is utilized and $\bar{\varepsilon}^p$ is the logarithmic plastic strain defined as:

$$\bar{\varepsilon}^p = \int (\tfrac{2}{3}D^p_{ij}D^p_{ij})^{1/2}\,dt. \tag{24}$$

Here D^p_{ij} is the plastic part of the rate of deformation tensor.

In a typical analysis, e.g. the proportional case, load level 4, 1300 load increments with roughly 3 equilibrium iterations per increment (Newton's method), were needed to reach the final load. This required about 7.7 CPU-hours on a HP-730 work station.

The resulting J-values vs the radial distance (in undeformed configuration) to the contour at which J has been calculated are shown in Fig. 4. Each diagram contains results for all three loading paths for a particular load level. All curves are scaled by the converged J-value based on the domain integral method for the proportional case, G_{prop}. The final values of the nondimensional loading parameter λ are given in Table 1. For the first load level the plastic zone is equal to $0.036 \times a$ for all load paths and the ASTM-condition for linear elastic fracture mechanics is fulfilled. For the remaining load levels the plastic zone has spread across the ligament, hence large scale yielding prevails for these load cases.

The differences between the results from the two methods, effectively corresponding to the second term in eqn (7), are small, within a few percent. They are not significantly

Table 2. Mean J and G values, of contours numbers 2–35, for the linear elastic text example (SEN)

	Mean value	Variation, %
$G/(\sigma_Y^2 a/E)$, (ABAQUS)	1.45633	0.11
$J/(\sigma_Y^2 a/E)$, (contour integral)	1.45652	0.32

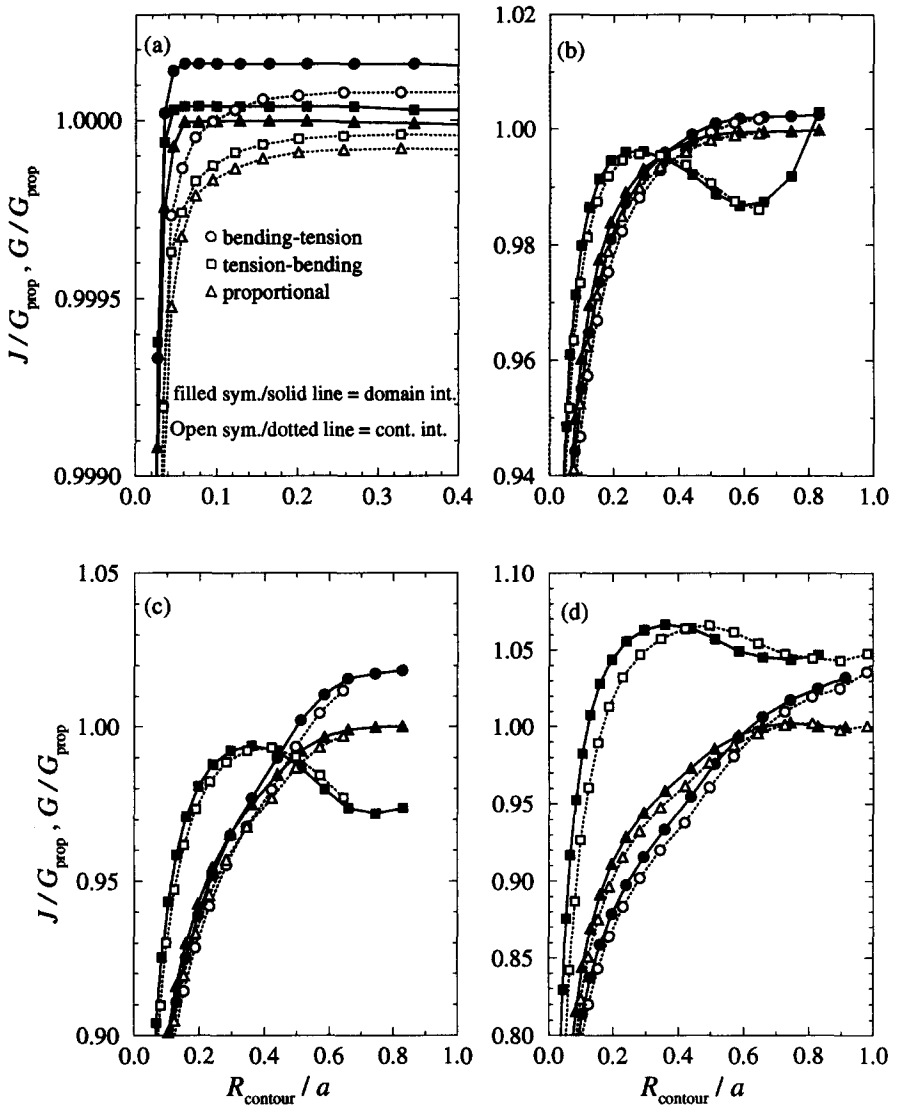

Fig. 4. J and G vs $R_{contour}$ at load levels (a) $\lambda \approx 1/1896$ ($G_{prop} = 0.2518(\sigma_Y^2 a/E)$), (b) $\lambda \approx 1/143$ ($G_{prop} = 3.5(\sigma_Y^2 a/E)$), (c) $\lambda \approx 1/28.8$ ($G_{prop} = 17.4(\sigma_Y^2 a/E)$) and (d) $\lambda \approx 1/12.1$ ($G_{prop} = 41.2(\sigma_Y^2 a/E)$).

larger for the nonproportional cases than for the proportional ones. It should be mentioned that the second term (nonzero if nonradial stressing) only involves the area over the ring of elements passed by the contour in question due to the choice of the q_1 function made in ABAQUS as mentioned above. Both methods appear to give the same remote converged J-values, though the remote J-values from the nonproportional tension–bending case varies somewhat. This could be explained by Fig. 3, where it can be seen in relation to the generalized yield surface that the tension–bending sequences exhibit a higher degree of nonproportional plastic loading than the other sequences do. This is also confirmed by checking the plastic displacements corresponding to the applied forces F and P, where the tension–bending sequences differ significantly from both the proportional and the bending–tension sequences. The latter ones agree fairly well with each other.

The general trend is that the J-values converge somewhat faster towards the remote values for the domain integral method than for the contour integral method as might be expected.

For all load levels the J-integral exhibits a significant path dependence immediately adjacent to the blunted crack tip. In fact the J_{tip}-value seemingly tends to zero. This is in agreement with findings by other authors when finite strains have been considered and has

been thoroughly discussed by McMeeking (1977b). McMeeking argues in the case of small-scale yielding that if an outer field, characterized by a path independent value of J, controls the deformation in an inner field in which J is path dependent, then the remote J-value is directly connected to the near-tip field. This has also been demonstrated for large-scale yielding in deeply cracked plane strain specimens by McMeeking and Parks (1979).

In the proportional cases J has reached 95% of the converged remote value on a contour at radial distances of $R \approx 11J/\sigma_Y$, $11J/\sigma_Y$, $5J/\sigma_Y$ and $3J/\sigma_Y$ for load levels 1, 2, 3 and 4 respectively. In the nonproportional tension–bending cases the rate of convergence is more rapid while in the nonproportional bending–tension cases the convergence is slightly slower.

At the lowest load level (Fig. 4), fulfilling the ASTM condition for linear elastic fracture mechanics, the order of load application has an insignificant effect on the remote J-values. The differences become larger for higher load levels and the trend is that a tension–bending sequence deviates from the other ones.

At the highest level considered it can be questioned whether the J-values for the bending–tension sequence have really converged to an unambiguous remote value. Here the size of the near-tip field is probably not negligible compared to the remaining ligament and it is dubious if a remote J-value is connected to the near-tip field.

When judging the differences it has to be kept in mind, however, that experimental determination of critical J-values seldom can be expected to yield a better accuracy than say $\pm 15\%$.

At the higher load levels, when path dependence in J is more pronounced, it is not so obvious what is due to finite strain effects and what is due to the influence of remotely applied nonproportional loads. To this end load level 3 was reanalysed using a small strain assumption (the mesh was the same). The resulting J-values, normalized in the same manner as before, versus contour radius are shown in Fig. 5. The remote behaviour resembles the results from the finite strain analysis. For instance in the proportional loading case, both finite strain and small strain analysis result in path independent J-values at contour radius greater than $0.5a$. However, one should observe that G_{prop} is roughly 22% higher in the small strain analysis than in the finite strain analysis. The reason for this is that the force P will cause a displacement in the positive X_1-direction of the load point. The bending moment due to the tensile force F will therefore decrease, which is accounted for in the finite strain analysis but not in the small strain analysis. One may also observe that the remote J-value in the tension–bending case is comparatively lower relative to the proportional case in the small strain analysis than in the finite strain analysis. When the tensile

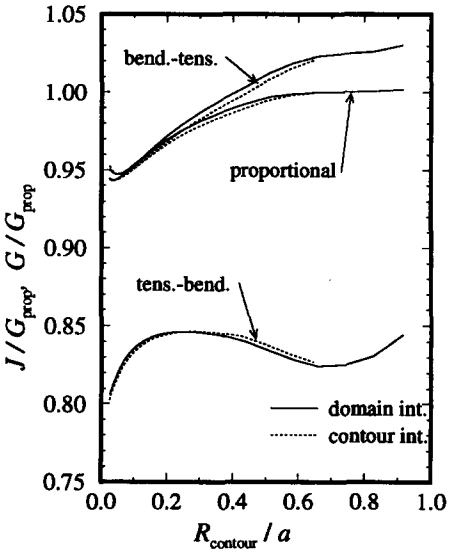

Fig. 5. J and G vs $R_{contour}$ from the small strain analysis corresponding to the load level 3 case. $G_{prop} = 21.3(\sigma_Y^2 a/E)$.

force F first is applied the load point is displaced in negative X_1-direction and thus the induced bending moment is increasing. This is again only accounted for in the finite strain analysis. In fact, J is a factor of 2.1 larger in the finite strain analysis at this first load step. Obviously J-results computed for "bending sensitive" structures loaded in tension can be remarkably different if large deformation is taken into account or not.

3.1.2. *Near-tip field characterization in plane strain.* In order to find the influence of the remotely applied nonproportional loads, the near-tip fields are examined within the framework of the J-Q theory (O'Dowd and Shih, 1991, 1992, hereafter referred to as OS). A brief review of the J-Q theory will be given below.

In OS the modified boundary layer formulation (MBL) was investigated. The remote tractions are given by the first two terms of the small-displacement-gradient linear elastic solution (Williams, 1957), as depicted in Fig. 6. By generating the full range of small-scale yielding solutions ($(\sigma_{ij})_{SSY}$), OS considered the difference field defined by:

$$\Delta\sigma_{ij} = (\sigma_{ij})_{SSY} - (\sigma_{ij})_{REF}, \tag{25}$$

where $(\sigma_{ij})_{REF}$ can be the HRR-field or $(\sigma_{ij})_{SSY;T=0}$. The latter could be regarded as a more natural choice, especially if the material is not strictly of power law type. This latter choice will be used in this study. By systematic investigation of the difference fields OS found that in the forward sector $|\theta| < \pi/2$ of the annulus $J/\sigma_Y < r < 5J/\sigma_Y$ the difference field displayed minimal dependence on r, leading to the simple form:

$$\Delta\sigma_{ij} = Q\sigma_Y\hat{\sigma}_{ij}(\theta). \tag{26}$$

Here the angular functions, $\hat{\sigma}_{ij}(\theta)$ are normalized by setting $\hat{\sigma}_{\theta\theta}(\theta = 0)$ equal to unity. Moreover, OS noted that in the forward sector, $\hat{\sigma}_{ij}(\theta)$ could approximately be replaced by δ_{ij}. Then, Q effectively corresponds to a spatially uniform hydrostatic stress in this sector, with the interpretation that it is a measure of near-tip stress triaxiality, or crack-tip constraint, relative to a reference high triaxiality field. In OS Q is defined by:

$$Q = \frac{\sigma_{\theta\theta} - (\sigma_{\theta\theta})_{SSY;T=0}}{\sigma_Y} \quad \text{at} \quad \theta = 0,\ r = 2J/\sigma_Y. \tag{27}$$

This definition is used to compute Q from the numerical solutions in the present study.

The crack-tip opening displacements, CTOD, defined by the opening where the 45° lines drawn backwards from the crack-tip intersect the deformed crack faces, can be written as:

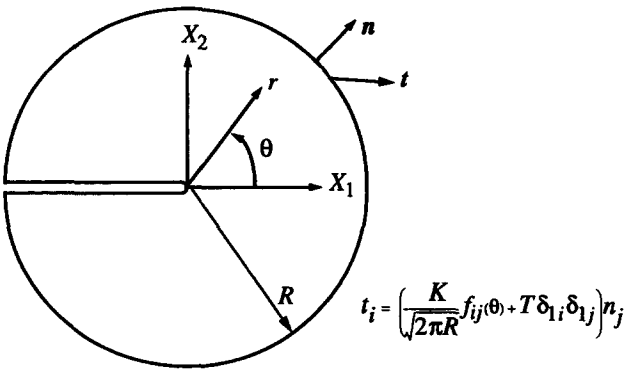

Fig. 6. Two-parameter boundary layer formulation (MBL).

$$\delta_t = d\frac{J}{\sigma_Y}, \tag{28}$$

where d is a function of Q and dimensionless combinations of material parameters. Now, OS denote the whole range of field solutions generated with the boundary layer formulation as a J-Q family of fields, where the Q-value particularizes a specific member of the family.

In this investigation Q is determined for each load level and each loading sequence for the SEN specimen. In addition MBL solutions—J-Q fields—are generated by choosing T/σ_Y to give the same Q-values as in the proportional loading sequences. The solutions of the SEN specimen will be compared with the MBL solution below.

The MBL model has a similar near-tip mesh as the one used for the SEN specimen shown in Fig. 2(c), but with an initial notch radius, ρ_0, equal to $0.83 \times 10^{-7}R$. Here R is the radius to the outer boundary of the MBL model [see Fig. 2(c)]. Small-scale yielding conditions are enforced by not allowing the plastic zone size to extend more than $0.01R$ from the initial notch. Furthermore the K-T field is applied, keeping the T/K ratio constant, as prescribed displacements corresponding to the tractions in Fig. 6.

Figure 7 shows how Q develops under increasing load for all loading sequences. Also included are the pure tension and the pure bending cases. The pure bending case is considered to be a highly constrained case, since Q is virtually zero until the loading gets very high, where Q decreases. On the contrary, the pure tension case is considered to be a lowly constrained case, since Q is decreasing with increasing load and at high load levels Q saturates at roughly -1.4. Obviously different loading paths must have separate Q vs λ, or J, histories. The bending–tension sequences implies going from a high to a lower constrained situation. The tension–bending sequencies implies going to a low and then to a somewhat more constrained situation. Finally at proportional loading Q is monotonically decreasing with increasing load. At the first load level ($\lambda \approx 1/1896$), the plastic zone is most likely embedded in a zone characterized by an elastic K-T field as applied to the MBL problem described above and small-scale yielding conditions should apply. If so, Q must depend on the applied forces (F and P) only, since in the small-scale yielding situation there is a one to one correspondence between T and Q (cf. OS; Betegon and Hancock, 1991). This indeed appears to be true.

In Figs 8–11 a concentrated representation of the stress and strain fields is given. In these figures r is the radial distance in undeformed configuration from the intersection point of the initial notch and the symmetry plane. Figure 8 shows the angular distribution of the

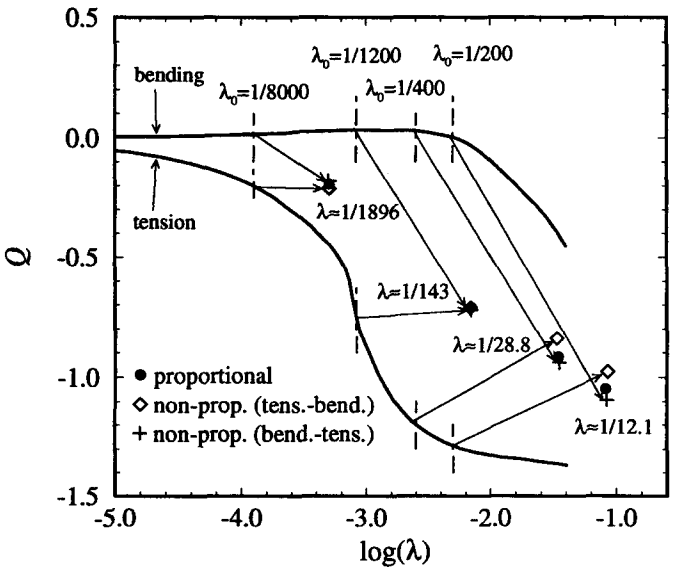

Fig. 7. Different loading paths for the SEN specimen having separate Q vs nondimensional loading parameter ($\lambda = J/(L\sigma_Y)$), or J, histories.

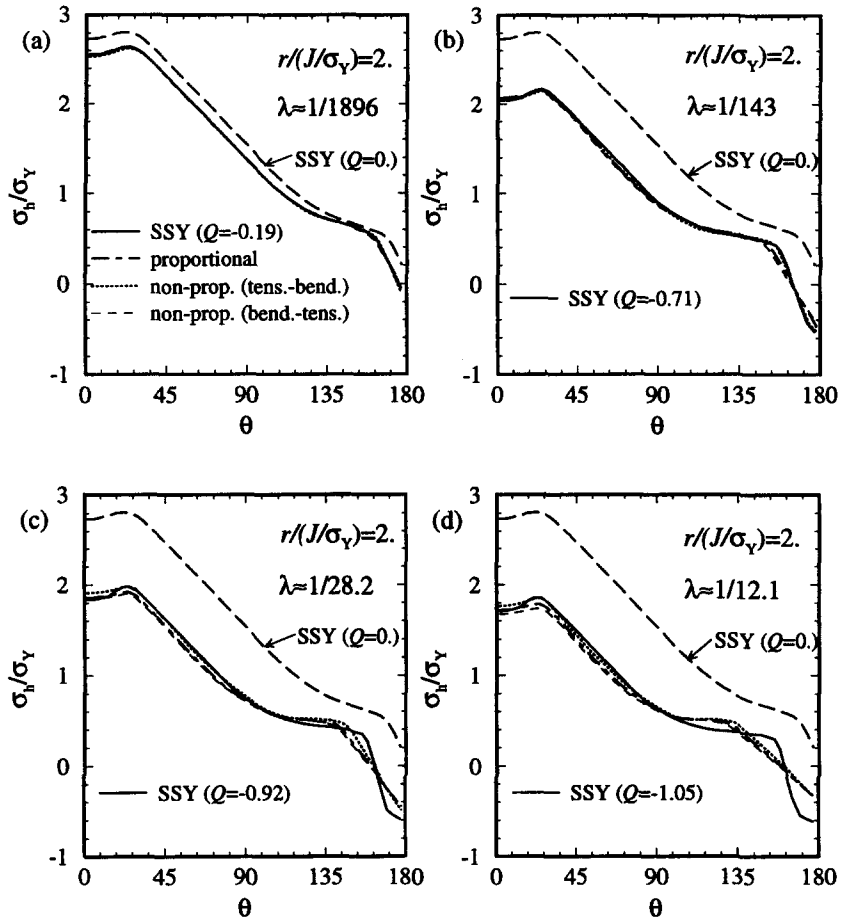

Fig. 8. Angular variation at $r/(J/\sigma_Y) = 2$ of hydrostatic stress, $\sigma_h = \sigma_{kk}/3$, for the MBL solution and for the SEN specimen with different loading sequences. Also included is the MBL ($Q = 0$)-solution. The load levels are (a) $\lambda \approx 1/1896$, (b) $\lambda \approx 1/143$, (c) $\lambda \approx 1/28.8$ and (d) $\lambda \approx 1/12.1$. The legends for the SEN specimen are shown in (a).

hydrostatic stress, denoted σ_h, at a radial distance of $2J/\sigma_Y$. The agreement with the MBL solution is excellent at the lowest load level in the whole range, as expected for reasons discussed above. At the higher load levels the agreement is still good at least in the forward sector. That the difference field is almost hydrostatic here is clear by comparison with the reference field ($(\sigma_h)_{SSY;T=0}$), also included.

The normal stress distribution ahead of the crack is shown in Fig. 9. The angle, $\theta = 1.6°$, corresponds to the element Gauss points closest to the symmetry plane. For the lowest load level the agreement with the MBL solution is extremely good for all loading sequences, as expected. For the remaining load levels, where large-scale yielding prevails, the σ_{rr} component is somewhat lower than in the MBL solution, implying that $\hat{\sigma}_{rr}(\theta \approx 0)$ is larger than unity and actually equal to 1.2. This is in accordance with OS, where similar results are reported in the case of large-scale yielding. When λ becomes large, the tension–bending sequence starts to deviate from the other loading sequences and has a slightly higher Q-value. At the highest load level all loading sequences deviate from the MBL solution. This could be explained by a bending induced stress gradient across the ligament. The hoop stress is compressive near the free surface opposing the crack tip. Note that here, the size of the ligament is equal to 12.1 (J/σ_Y).

The radial variation of the equivalent plastic strain at $\theta = 43.4°$ is shown in Fig. 10. The conformity with the MBL solution is notable at the lowest load level. At higher load levels the different loading sequences agree reasonably well with each other, but the deviations from the MBL solution is significant. This discrepancy is not unexpected since

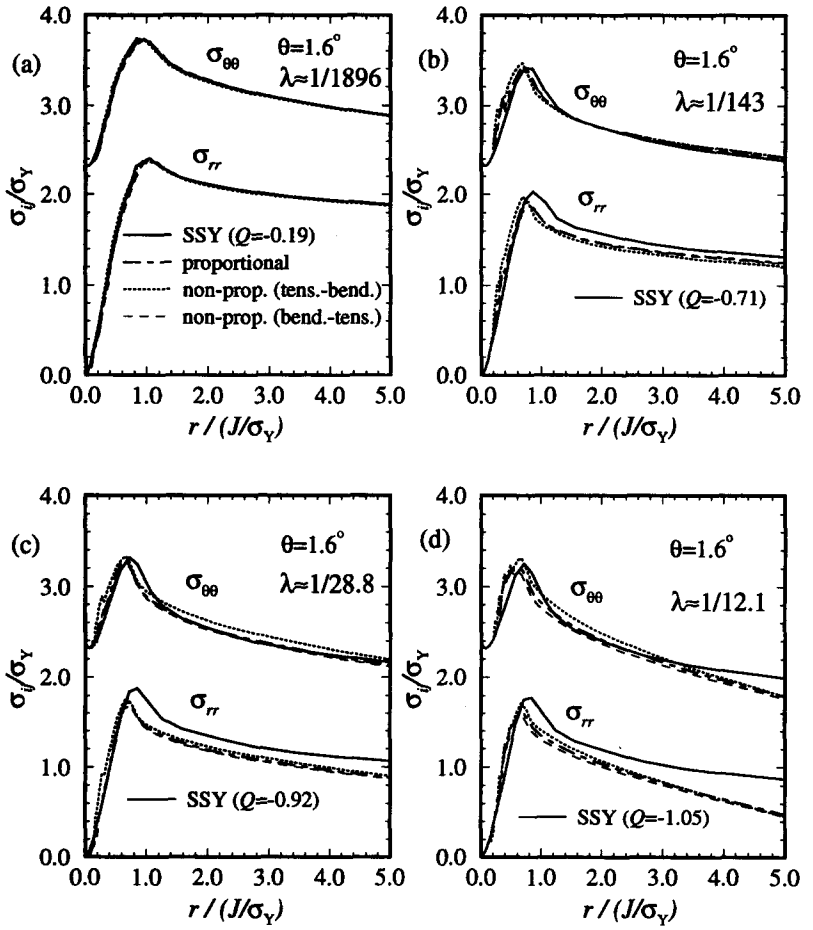

Fig. 9. Comparison of normal stresses ahead of the crack tip ($\theta = 1.6°$) between the MBL-solution and different loading paths for the SEN specimen. The load levels are (a) $\lambda \approx 1/1896$, (b) $\lambda \approx 1/143$, (c) $\lambda \approx 1/28.8$ and (d) $\lambda \approx 1/12.1$. The legends for the SEN specimen are shown in (a).

a small deviation from the MBL stresses, as observed above, is magnified in strains [$\bar{\varepsilon}^p \propto (\bar{\sigma}/\sigma_Y)^n$]. However, very close to the blunted crack tip all solutions fall close together. The reason for this is that here the influence of Q is minimal. In fact $Q \to 0$ when $r \to 0$ as can be seen in Fig. 9, and the plastic deformation is determined by J alone.

The angular variation of equivalent plastic strain at a radial distance equal to $2J/\sigma_Y$ is shown in Fig. 11. In order to examine the influence of Q, the reference field ($(\bar{\varepsilon}^p)_{SSY;T=0}$) is also included. Again all loading sequences coincide with the MBL solution at the lowest load level, but at the higher load levels the discrepancies are considerable. Here the difference could be referred to as an offset in phase and the plastic deformation is pushed towards the symmetry plane ($\theta = 0$). Note that the maximum value from the SEN specimen solutions does not diverge more than 10% from the maximum value from the MBL solution at each load level. As can be seen the different loading sequences agree well with each other, except at the highest load level, where also the Q-values from the tension–bending and the bending–tension sequences respectively deviate somewhat from the proportional sequence as can be seen in Fig. 9(d).

The crack tip opening, δ_t, is computed from the numerical solutions as described above and the function d is estimated in accordance with eqn (28). In Fig. 12, d is plotted against Q for all loading sequences and compared with the MBL solution. At Q equal to zero, d is equal to 0.42. This is somewhat lower than 0.44, which McMeeking (1977a) reported using the same type of material law, but with a larger σ_Y/E ratio and this could account for at least some of the discrepancy. At lower load levels, corresponding to higher Q-values, the proportional loading sequence agrees very well with the MBL solution. Here, the trend is that the tension–bending sequence has a slightly lower d value and the bending–tension

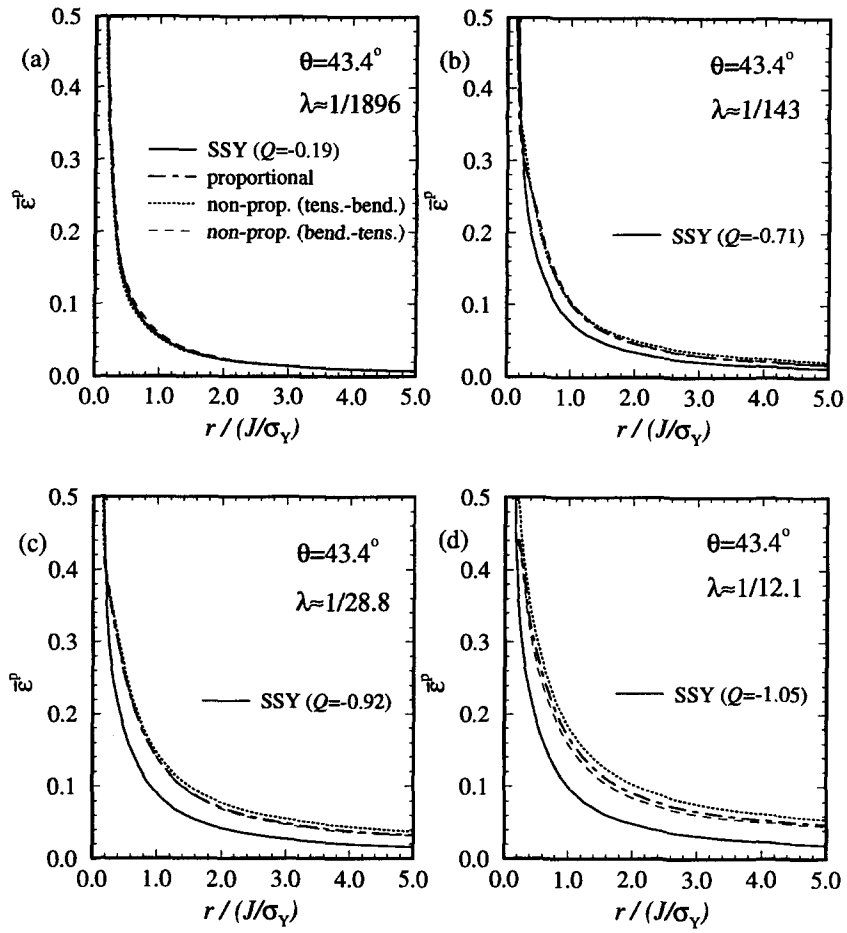

Fig. 10. The equivalent plastic strain $\bar{\varepsilon}^p$ vs $r/(J/\sigma_Y)$ at $\theta = 43.4°$ for the MBL-solution and the SEN specimen with different loading paths. The load levels are (a) $\lambda \approx 1/1896$, (b) $\lambda \approx 1/143$, (c) $\lambda \approx 1/28.8$ and (d) $\lambda \approx 1/12.1$. The legends for the SEN specimen are shown in (a).

sequence has a slightly higher d value than the MBL solution. At the higher load levels the proportional sequence and especially the bending–tension sequence starts to deviate from the MBL solution.

3.2. *Example 2: combined bending and tension in a three-dimensional specimen*

In this second example a plate specimen with a semi-elliptical surface crack (SCT) is studied, as depicted in Fig. 13. Figure 14 shows the finite element model used (only a quarter of the full body is modelled for symmetry reasons) and the definition of a dimensionless parameter s which defines the position along the crack front. The circular tube embracing the crack front contains 492 elements divided in 12 slices and the remaining part includes 1110 elements. Here the midnodes are placed on the ellipses and hyperbolas forming the mesh in this region. For the elastic–plastic analysis the initial notch radius, ρ_0, is $0.93 \times 10^{-3}a$. The face opposing the crack surface is constrained to remain on a plane.

3.2.1. *Results: combined bending and tension in a three-dimensional specimen.* Also in this case a linear elastic ($\nu = 0.3$) analysis is performed to test the implemented J-integral routine. A combination of N and M, see Fig. 13, is chosen to give pure tension at the cracked plane. An average J-value in each element slice is calculated from contours passing through the 2nd to the 9th element ring surrounding the crack tip. This together with the variation around the mean value are shown in Table 3. The agreement between the methods is extremely good, the difference is of the same order as the variation around the mean value for the contour integral method.

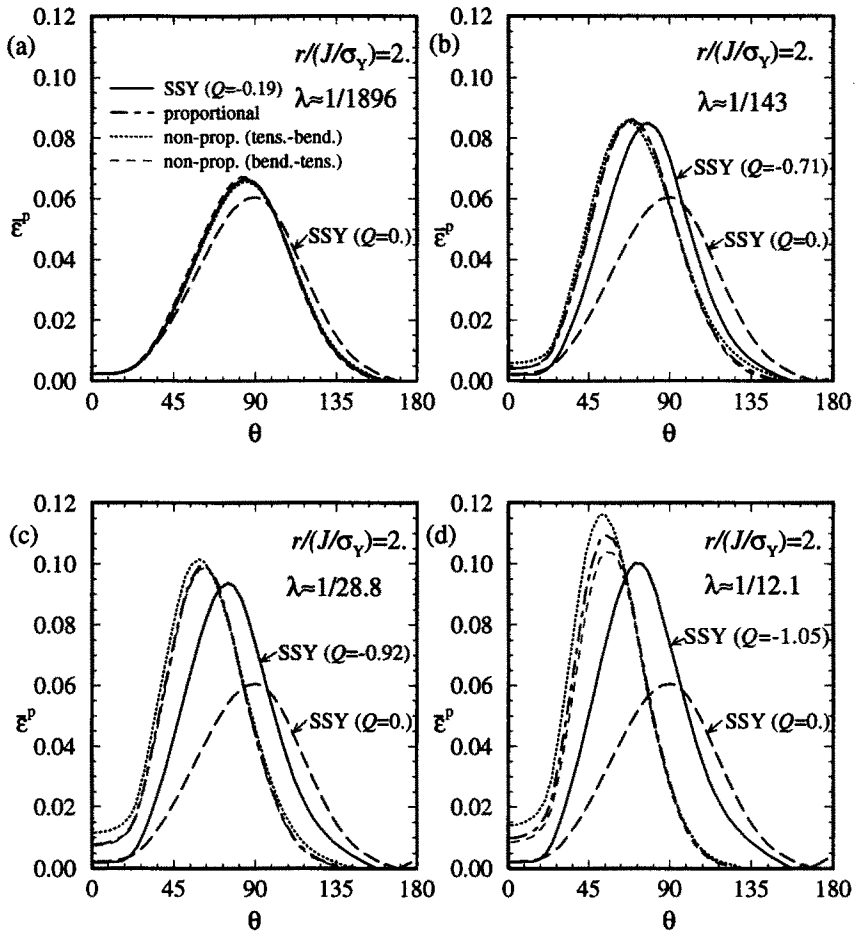

Fig. 11. Angular variation at $r/(J/\sigma_Y) = 2$ of the equivalent plastic strain $\bar{\varepsilon}^p$ for the MBL-solution and the SEN specimen with different loading paths. The load levels are (a) $\lambda \approx 1/1896$, (b) $\lambda \approx 1/143$, (c) $\lambda \approx 1/28.8$ and (d) $\lambda \approx 1/12.1$. The legends for the SEN specimen are shown in (a).

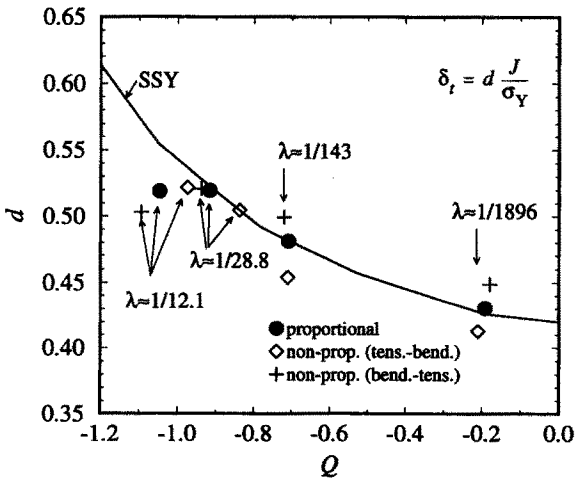

Fig. 12. The function d (in the CTOD expression) for the SEN with different loading sequences at various load levels, λ, compared with the MBL solution.

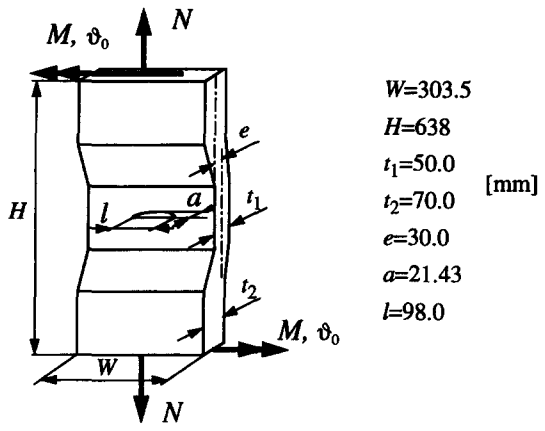

Fig. 13. The three-dimensional bending–torsion example investigated—SCT specimen.

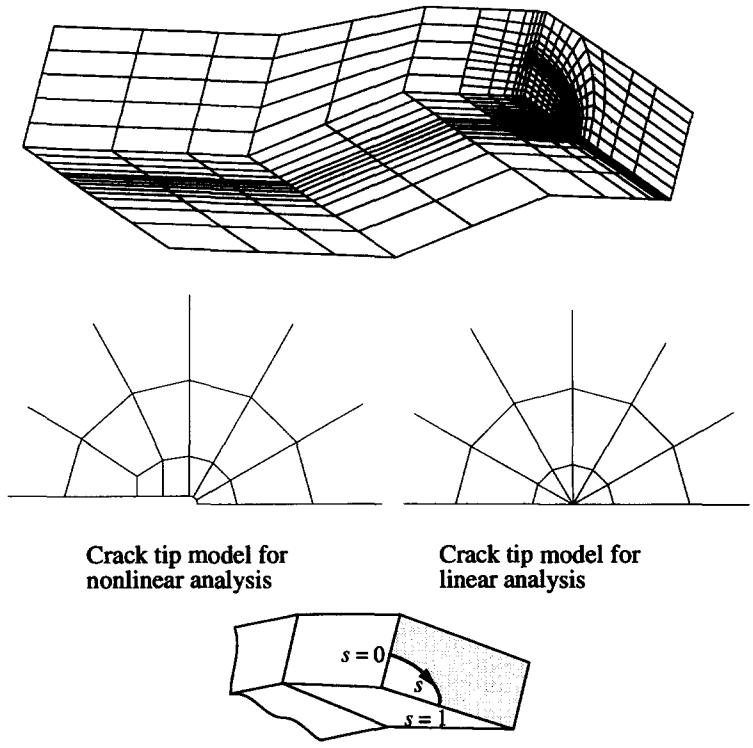

Fig. 14. Finite element model of a quarter of the SCT specimen, different crack tip meshes and definition of the parameter s.

If instead the pointwise values from the domain integral method are checked, a small path dependence is detected when the free surface ($s = 1$) is approached. The trend for this path dependence is that G increases slightly with increasing contour radius evaluated on midnodes and G decreases slightly with increasing contour radius evaluated on vertex nodes.

Table 3. Mean J and $\bar{G}$ values, of contours numbers 2–9, along the crack front for the linear elastic test example (SCT)

Position s	0.056	0.166	0.275	0.371	0.480	0.573	0.659	0.737	0.807	0.869	0.925	0.976
$\bar{G}/(\sigma_Y^2 a/E)$	0.2010	0.1989	0.1944	0.1880	0.1797	0.1697	0.1585	0.1466	0.1350	0.1254	0.1205	0.1251
Variation %	0.041	0.040	0.038	0.035	0.028	0.028	0.033	0.043	0.045	0.068	0.071	0.16
$J/(\sigma_Y^2 a/E)$	0.2013	0.1991	0.1948	0.1884	0.1801	0.1701	0.1588	0.1470	0.1354	0.1258	0.1209	0.1260
Variation %	0.37	0.38	0.37	0.37	0.37	0.36	0.35	0.32	0.27	0.23	0.30	1.10

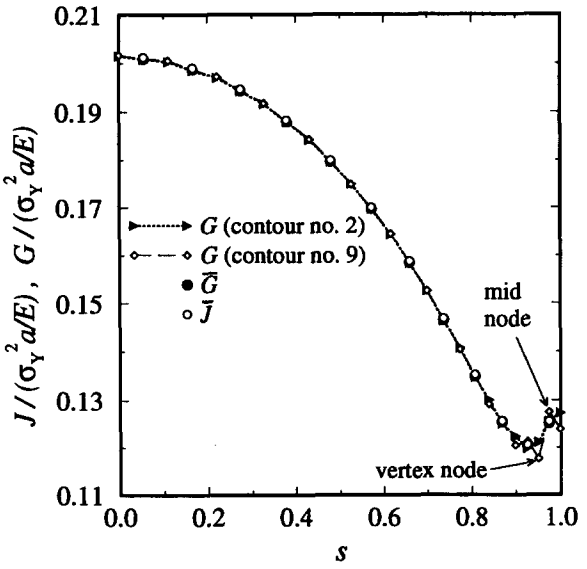

Fig. 15. Linear elastic test (SCT specimen) showing element averaged J-values ($\bar{J}$) from contour integration, element averaged J-values ($\bar{G}$) and pointwise J-values of contours number 2 and number 9 from domain integration vs position, s, along the crack front.

This is illustrated by plotting pointwise G-values vs crack front position, s, choosing contour number 2 (close to the crack front, $R_2 \approx 0.01a$) and contour number 9 (remote from the crack front, $R_9 \approx 0.5a$), as shown in Fig. 15. Here, the element average values are also included for comparison. Note that the pointwise J-values from contour number 9 start to oscillate around $\bar{G}$ when $s \to 1$, while this is not the case for contour number 2. This problem is probably due to large gradients in the field variables tangential to the crack front and the mesh is most likely to be too coarse close to the free surface. This effect is obviously very small if an averaged J-value ($\bar{G}$) is calculated.

The elastic–plastic finite strain calculations are carried out for a material with $\nu = 0.3$, $\sigma_Y/E = 1/798$ and where the hardening properties in eqn (15), given as the yield function, are shown in Fig. 16. If a fit of eqn (22) to the data in Fig. 16 is done the hardening parameter, n, will roughly be 5. The nonproportional load is applied as follows: The specimen is first given an initial bending moment $\hat{M}_0$ by rotating the ends an angle ϑ_0, see Fig. 13. It is then loaded in tension, keeping ϑ_0 constant. Here a hat (ˆ) denotes resulting forces or moments in the crack plane. The loading is depicted in Fig. 17 as $\hat{M}$ and $\hat{N}$, scaled with the respective limit loads without a crack. The initial moment $\hat{M}_0$ is large enough to give plastic deformation in the body even without a crack.

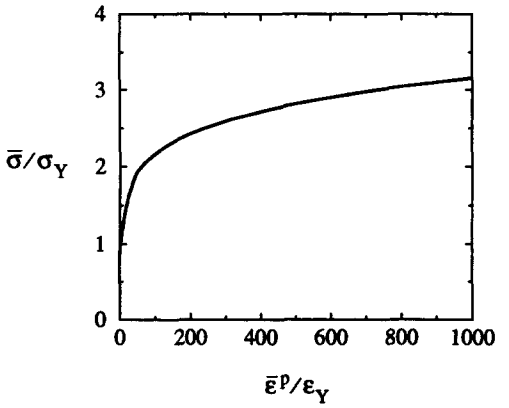

Fig. 16. Yield function for the three-dimensional elastic–plastic analysis: Cauchy stress vs logarithmic plastic strain.

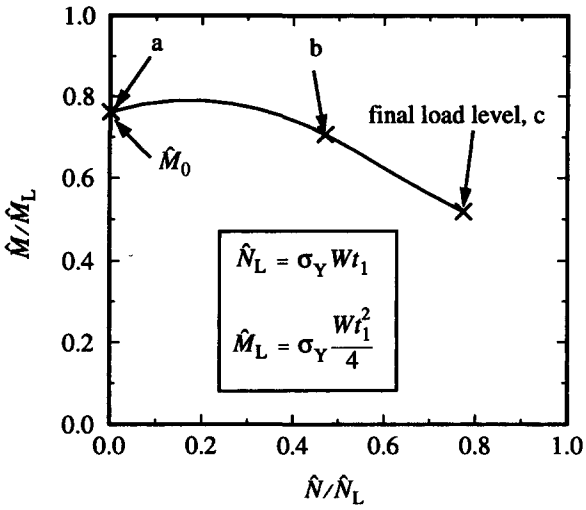

Fig. 17. Loading sequence for the SCT specimen.

This problem was solved on a CRAY-XMP main frame computer and the final load level was reached in 101 load steps requiring 314 equilibrium iterations (Newton's method) and in total 35.4 CPU-hours were needed.

With the linear elastic results in mind, the potential deviation in average J-values between the methods should depend on the degree of nonproportionality of the loading. We will focus our attention on three positions along the crack front, $s = 0.056$, $s = 0.573$ and $s = 0.925$, to get a condensed picture of the overall behaviour. J-values averaged over one element slice are presented in Table 4 for the final load level, where $\lambda_{max} \approx 1/24$. In the expression of λ, eqn (19), L is taken as the crack depth a in Fig. 13. Here contours from the 2nd to the 8th element ring are included (only to the 7th element ring for the contour integral method, since unfortunately no more data were saved during the FEM analysis). The results for positions $s = 0.056$ and $s = 0.925$ are also shown in Fig. 18a. In this three-dimensional case as well as in the two-dimensional case, a significant path dependence immediately adjacent to the blunted crack tip is apparent, as discussed in Section 3.1.1.

The agreement between the methods is very good with the same trend as for the two-dimensional results that the domain integral values tend to the remote values quicker than the contour integral values. For both methods 95% of the remote value is reached at a contour at a radial distance, measured in the undeformed configuration, of roughly $2J/\sigma_Y$. This is valid along the whole crack front based on element slice average values.

Table 4. $\bar{J}$ and $\bar{G}$ values at different contour radii at three locations along the crack front for the elastic–plastic finite strain analysis (SCT)

	Contour	2	3	4	5	6	7	8
$s = 0.056$	$R_{contour}/a$	0.0134	0.0298	0.0606	0.117	0.219	0.345	0.509
	$\bar{G}/(\sigma_Y^2 a/E)$	25.97	28.65	29.97	30.68	31.16	31.57	32.09
	$R_{contour}/a$	0.0112	0.0255	0.0523	0.102	0.191	0.310	—
	$\bar{J}/(\sigma_Y^2 a/E)$	22.48	26.84	29.13	30.23	30.87	31.27	—
$s = 0.573$	$R_{contour}/a$	0.0108	0.0241	0.0490	0.0951	0.179	0.282	0.420
	$\bar{G}/(\sigma_Y^2 a/E)$	25.03	28.53	30.44	31.40	31.88	32.24	32.48
	$R_{contour}/a$	0.0090	0.0206	0.0423	0.0825	0.156	0.272	—
	$\bar{J}/(\sigma_Y^2 a/E)$	21.08	26.09	29.21	30.80	31.60	32.04	—
$s = 0.925$	$R_{contour}/a$	0.0064	0.0142	0.0292	0.0574	0.111	0.177	0.274
	$\bar{G}/(\sigma_Y^2 a/E)$	17.01	20.37	22.73	23.90	24.06	24.18	24.16
	$R_{contour}/a$	0.0053	0.0121	0.0251	0.0496	0.095	0.163	—
	$\bar{J}/(\sigma_Y^2 a/E)$	14.69	19.06	21.35	22.38	23.11	23.87	—

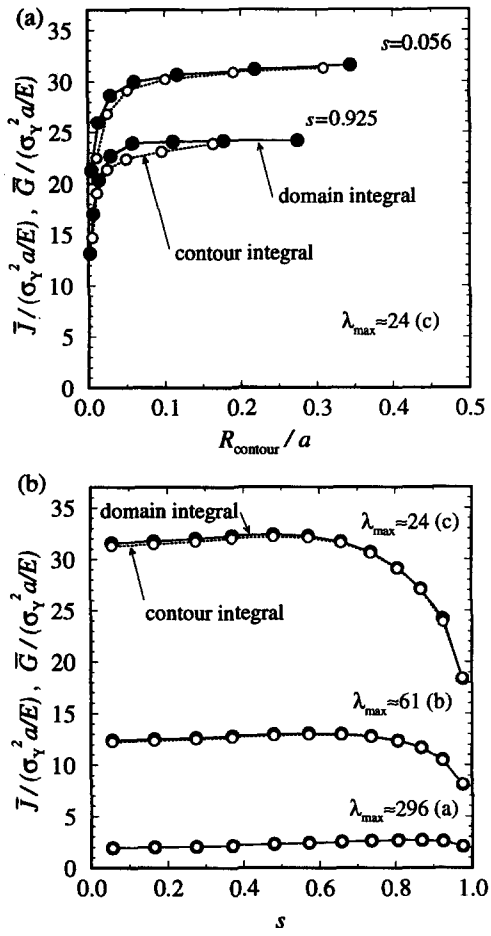

Fig. 18. Element average J-values, $\bar{J}$ (contour integral) and $\bar{G}$ (domain integral) for the SCT specimen (a) vs R_{contour} at two locations along the crack front and (b) vs position, s, along the crack front, where the remote contour is used in both methods.

Choosing contour number 7, the variation of $\bar{J}$ and $\bar{G}$ along the crack front, normalized by $\sigma_Y^2 a/E$, can be seen in Fig. 18(b), where the corresponding load levels, a, b and c, are depicted in Fig. 17. If expressed in the nondimensional loading parameter they compare to $\lambda_{a,\max} \approx 1/296$, $\lambda_{b,\max} \approx 1/61$ and $\lambda_{c,\max} \approx 1/24$. No significant disagreement can be observed.

3.3. *Example 3: simulated crack growth in three dimensions*

The last example deals with simulation of crack propagation (mode I) in a 20% side-grooved CT-specimen. The geometry of the specimen as well as the finite element model of the quarter-body (symmetry) are shown in Fig. 19. The model has six element layers across the half-thickness, four of which are located at the crack front and two in the side-grooved zone. The circular region in each layer contains 119 elements, divided in 12 circular rings, and in total the model includes 1278 elements. Remote from the crack the mesh is coarser and consists of only three layers. Appropriate symmetry conditions are employed and the load is applied by uniform prescribed transverse displacements for nodes lying on a line depicted in Fig. 19. The normalized distance along the crack front, s, is expressed by $s = X_3/2B_N$, where B_N is the net thickness of the specimen. The crack front is slightly curved and has a parabolic continuous shape, symmetric with respect to $X_3 = 0$. The initial crack length, $a_0(s)$, is equal to $0.613W$ at $s = 0$ and equal to $0.594W$ at $s = \pm 1$. The crack growth, Δa, is uniform along the crack front and at the final load Δa is $0.0456W$.

3.3.1. *Results: simulated crack growth in three dimensions.* The crack growth history is chosen to comply roughly with a linear J_R-curve expressed by:

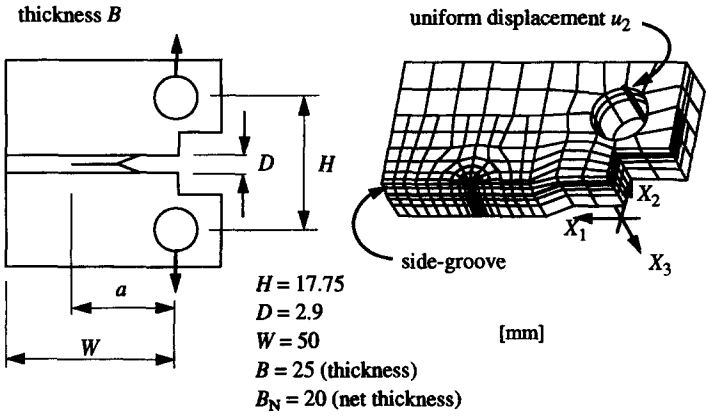

Fig. 19. The three-dimensional crack growth example investigated—CT specimen: geometry and finite element model of a quarter of the specimen.

$$J_R/(\sigma_Y^2 L/E) = \alpha + \beta(\Delta a/L), \tag{29}$$

where α and β are dimensionless constants. Specifically $\beta \approx 1.08 \times 10^3$, and $L = W - a_0 (s = 0)$. The growth is simulated by means of a nodal relaxation technique, where the solution is divided into 12 steps with increasing load. Crack growth is initiated at the end of the third step and for each following step, nodes ahead of the crack front are released. The crack growth, Δa, at some steps is shown in Table 5. The mesh is so constructed that the crack growth is measured in the deformed configuration at a load level corresponding to crack growth initiation. In Table 5 also the load levels in terms of λ are shown for the different steps. In the expression of λ, eqn (19), J is taken as the remote value in the element layer adjacent to the symmetry plane.

An element average J-value, as described previously, is calculated at circular paths surrounding the initial crack front. Consequently, contours passed by the propagating crack will be omitted. The "radial" length to a contour will then be taken as the distance between the propagating crack front and the contour in question ahead of the crack front.

The material assumptions are the same as in the previous three-dimensional example and an elastic–plastic finite strain analysis is undertaken.

The problem was solved by taking 325 load increments, with about three equilibrium iterations in each increment, requiring 157 CPU-hours on a HP-730 work station.

Up to crack growth initiation, step 3, the loading can be considered as proportional and both methods should yield the same converged remote J-value. This is indeed the case as can be seen in Table 6 and in Fig. 20(a), where results are given for the first element layer ($s = 0.25$). The picture is the same in all layers except in the layer adjacent to the side-groove, which will be commented upon below. When the crack starts to propagate both methods give the same remote values which appears to be path independent, at least for small amounts of growth, see Table 6 and Fig. 20(b). For large amounts of growth, however, the remote values do not seem to converge to a path independent value, and significant differences between the methods can be observed. At this instance the load level is so high that the near-tip field, of order J/σ_Y, is a sizeable fraction of the remaining ligament and it is questionable if there exists a remote J-characterized field controlling the crack growth.

Table 5. Crack growth, the load level λ and the parameter ω, for different solution steps (CT)

Step number	→3	8	10	12
$\Delta a/W$	0.0	0.0128	0.025	0.0456
λ	≈1/19	≈1/10	≈1/6.5	≈1/4.7
ω	26	14	8.7	6.4

Table 6. $\bar{J}$ and $\bar{G}$ at different contour radii at position $s = 0.25$, for the crack growth example (CT)

$\lambda \approx 1/19$	$R_{contour}/L$	0.173	0.235	0.306	0.367	0.507	—
	$\bar{G}/(\sigma_Y^2 L/E)$	39.57	39.96	40.28	40.65	40.76	—
	$R_{contour}/L$	0.163	0.221	0.290	0.377	0.483	0.612
	$\bar{J}/(\sigma_Y^2 L/E)$	39.48	39.94	40.24	40.58	40.83	40.98
$\lambda \approx 1/10$	$R_{contour}/L$	0.131	0.193	0.264	0.355	0.465	—
	$\bar{G}/(\sigma_Y^2 L/E)$	69.52	72.28	74.50	76.64	78.02	—
	$R_{contour}/L$	0.121	0.179	0.248	0.335	0.441	0.570
	$\bar{J}/(\sigma_Y^2 L/E)$	66.92	70.69	72.92	75.19	77.08	78.38
$\lambda \approx 1/6.5$	$R_{contour}/L$	0.0996	0.162	0.233	0.323	0.434	—
	$\bar{G}/(\sigma_Y^2 L/E)$	99.42	106.35	112.26	117.61	121.52	—
	$R_{contour}/L$	0.0892	0.148	0.217	0.304	0.410	0.539
	$\bar{J}/(\sigma_Y^2 L/E)$	92.89	102.14	107.75	113.83	118.70	122.25
$\lambda \approx 1/4.7$	$R_{contour}/L$	0.0465	0.108	0.180	0.270	0.380	—
	$\bar{G}/(\sigma_Y^2 L/E)$	114.50	129.31	142.81	154.80	164.44	—
	$R_{contour}/L$	0.0361	0.0945	0.164	0.250	0.357	0.486
	$\bar{J}/(\sigma_Y^2 L/E)$	101.19	119.90	132.17	146.80	157.27	166.12

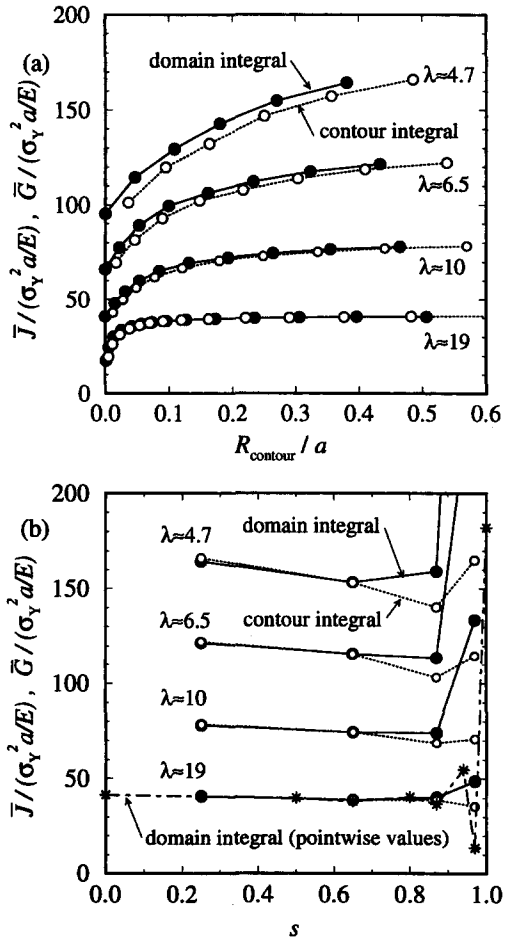

Fig. 20. Average J-values, $\bar{J}$ (contour integral) and $\bar{G}$ (domain integral) for the CT specimen (a) vs $R_{contour}$ at two locations along the crack front and (b) versus position, s, along the crack front, where the remote contour is used in both methods. Here the pointwise J-values of the domain integral are included.

In addition Hutchinson and Paris (1979) have suggested the following condition for J-controlled crack growth:

$$\omega = \frac{L}{J}\frac{\mathrm{d}J}{\mathrm{d}a} \geqslant \omega_c. \tag{30}$$

For CT specimens some authors suggest that $\omega_c > 5$ to 7 could be sufficient (cf. Hutchinson, 1983). In Table 5 ω is given for the considered load levels. It is of the same order as $1/\lambda$ and for the highest load level, corresponding to the largest crack growth, ω is roughly equal to the suggested value for ω_c.

Using the last contour from each method, element average values versus position s along the crack front for the four load levels, indicated in Table 6, are shown in Fig. 20. The general trend is an abrupt increase in J close to the side-groove. This has also been observed in other investigations of side-grooved CT-specimens (cf. Lorenzi and Shih, 1983; Shivakumar and Newman, 1992). Good agreement between the methods can be seen in the mid-section of the specimen, while closer to the side-groove there is a significant deviation. Here the same type of path dependence of the pointwise J-values from the domain integral method is observed as in the linear elastic example with the SCT specimen above. By plotting the G-values from the last contour, for $\lambda \approx 1/19$, severe oscillations can be seen in Fig. 20. The oscillations are probably due to the strong gradient in the field variables in the Z-direction (transverse), emanating from the side-groove. The finite element mesh adjacent to the side-groove is probably too coarse.

4. DISCUSSION AND CONCLUSIONS

By a direct comparison of the integral expressions from the two methods for J-evaluation, the difference, in both two-dimensions and three-dimensions, are terms which will vanish if the stressing is proportional. This is well known from previous studies.

In the two-dimensional example, no significant difference was found in the results from the two J-integral evaluation methods, even for strongly non-proportional loads. Different loading paths gave roughly the same remote J-value. In this example the near-tip stress and strain fields were carefully investigated. If a path independent remote J-value can be found, the main question is whether the solution, defined as a point in the J-Q space, will depend on the history before this point is reached (subjected to the restriction that J should be monotonically increasing). One can argue in this case that specimens having different J-Q histories should still have the same J-stress deviator histories, since the differences in the stress fields are restricted to a deviation in the hydrostatic stress, at least in the forward sector. Under small-scale yielding conditions the different loading sequences, giving rise to different J-Q paths, did not influence the stress and strain fields and a good correspondence with the MBL solution was found. That different J-Q paths to a final point in the J-Q space have a minimal influence on the near-tip fields under SSY-conditions, is indicated by O'Dowd and Shih (1991, 1992), who found that the solution was independent of which T/K ratio that was applied on the MBL problem. This appears to be true also in the large-scale yielding situations examined. The different loading sequences, corresponding to separate J-Q histories, agree well with each other and these stress fields coincide well with the MBL solutions, at least in the forward sector, $|\theta| < \pi/2$. However, the strain fields deviate from the MBL solution with a clear pattern. The high plastic straining is "pushed" towards the plane of symmetry. This, however, appears to have little influence on the CTOD. If the fracture mechanism is depending on high principal stresses (favouring cleavage fracture), then the observed differences in plastic strain fields should have no effect on a J-Q based fracture criterion. On the other hand, if large plastic straining is the primary fracture mechanism (favouring ductile fracture), then the observed differences in plastic strain fields could affect the applicability of a J-Q based fracture criterion.

In the three-dimensional examples, the SCT specimen subjected to combined bending–tension and the CT specimen with simulated crack growth, no significant difference between

the results from the methods of calculating the J-integral was found if an element average value of J was calculated. However, when the pointwise J-values from the domain integral method were checked, a small path dependence was found and it was specially marked if a strong gradient in the fields tangentially to the crack front existed, like close to the side-groove in the CT specimen. It is suspected that this is due to an insufficient finite element mesh in regions where this path dependence is observed.

Furthermore it was found that the domain integral method gives faster convergence towards the remote J-value than the contour integral method, although the difference is of minor practical importance.

Acknowledgement—The work was performed within the project "Computational methods for moving interior boundaries in solids and structures" granted by the Swedish Council for Engineering Research.

The authors are grateful to Professor F. Nilsson for initiating the investigation and for fruitful discussions and to Mr J.-M. Battini who carried out parts of the computer coding for the J-integral routines. Some of the numerical calculations were performed using the CRAY-XMP resources provided by the National Supercomputer Center (NSC). This support is gratefully acknowledged.

REFERENCES

ABAQUS (1989). *User's and Theory Manuals, Version 4.9*. Hibbitt, Karlsson and Sorensen, Inc. (HKS), Providence, RI.

Amazigo, J. C. and Hutchinson, J. W. (1977). Crack-tip fields in steady crack-growth with linear strain-hardening. *J. Mech. Phys. Solids* **25,** 81–97.

Bakker, A. (1984). On the numerical evaluation of J in three dimensions. In *Proc. Int. Conf. Applications of Fracture Mechanics to Materials and Structures* (Edited by G. C. Shih, E. Sommer and W. Dahl), pp. 657–667. Martinus Nijhoff Publishers.

Barsoum, R. S. (1977). Triangular quarter-point elements as elastic crack tip elements. *Int. J. Numer. Meth. Engng* **11,** 85–98.

Betegon, C. and Hancock, J. W. (1991). Two-parameter characterization of elastic-plastic crack-tip fields. *J. Appl. Mech.* **58,** 104–110.

Budiansky, B. and Rice, J. R. (1973). Conservation laws and energy-release rates. *J. Appl. Mech.* **40,** 201–203.

Carpenter, W. C., Read, D. T. and Dodds, R. H., Jr (1986). Comparison of several path independent integrals including plasticity effects. *Int. J. Fracture* **31,** 303–323.

Du, Z.-Z. and Hancock, J. W. (1991). The effect of non-singular stresses on crack-tip constraint. *J. Mech. Phys. Solids* **39,** 555–567.

Eshelby, J. D. (1970). Energy relations and the energy-momentum tensor in continuum mechanics. In *Inelastic Behaviour of Solids* (Edited by M. F. Kanninen, W. F. Adler, A. R. Rosenfield and R. I. Jaffee), pp. 77–115. McGraw-Hill Series in Material Science and Engineering, New York.

Hutchinson, J. W. and Paris, P. C. (1979). Stability analysis of J-controlled crack-growth. In *First Int. Symp. on Elastic Plastic Fracture Mechanics* (Edited by J. D. Landes, J. A. Begley and C. A. Clarke), pp. 37–64. ASTM STP 668.

Hutchinson, J. W. (1983). Fundamentals of the phenomenological theory of nonlinear fracture mechanics. *J. Appl. Mech.* **50,** 1042–1051.

Hughes, T. J. R. and Winget, J. (1980). Finite rotation effects in numerical integration of rate constitutive equations arising in large-deformation analysis. *Int. J. Numer. Meth. Engng* **12,** 1862–1867.

Li, F. Z., Shih, C. F. and Needleman, A. (1986). A comparison of methods for calculating energy release rates. *Engng Fract. Mech.* **21,** 405–421.

Lorenzi, H. G. and Shih, C. F. (1983). 3-D Elastic–plastic investigation of fracture parameters in side-grooved compact specimen. *Int. J. Fracture* **21,** 195–220.

McClintock, F. A. (1971). Plasticity aspects of fracture. In *Fracture: An Advanced Treatise, Volume III* (Edited by H. Liebowitz), pp. 47–225. Academic Press, New York.

McMeeking, R. M. (1977a). Finite deformations analysis of crack-tip opening in elastic–plastic materials and implication for fracture. *J. Mech. Phys. Solids* **25,** 357–381.

McMeeking, R. M. (1977b). Path dependence of the J-integral and the role of J as a parameter characterizing the near-tip field. In *Flaw Growth and Fracture*, pp. 28–41. ASTM STP 631.

McMeeking, R. M. and Parks, D. M. (1979). On criteria for J-dominance of crack tip fields in large-scale yielding, in elastic–plastic fracture. In *Elastic–Plastic Fracture* (Edited by J. D. Landes, J. A. Begley and C. A. Clarke), pp. 175–194. ASTM STP 668.

McMeeking, R. M. and Rice, J. R. (1975). Finite-element formulations for problems of large elastic-plastic deformation. *Int. J. Solids Structures* **11,** 601–616.

Moran, B. and Shih, C. F. (1987). Crack tip and associated domain integrals from momentum and energy balance. *Engng Fract. Mech.* **27,** 615–642.

Moran, B., Ortiz, M. and Shih, C. F. (1990). Formulation of implicit finite element methods for multiplicative finite deformation plasticity. *Int. J. Numer. Meth. Engng* **29,** 483–514.

Nagtegaal, J. C., Parks, D. M. and Rice, J. R. (1977). On numerically accurate finite element solutions in the fully plastic range. *Comput. Meth. Appl. Mech. Engng* **4,** 153–177.

Nakamura, T., Shih, C. F. and Freund, L. B. (1985). Computational methods based on an energy integral in dynamic fracture. *Int. J. Fracture* **27,** 229–243.

Nilsson, F. and Ståhle, P. (1988). Crack growth criteria and crack tip models. *SM Archives* **13**(4), 193–238.

O'Dowd, N. P. and Shih, C. F. (1991). Family of crack-tip fields characterized by a triaxiality parameter—I. Structure of fields. *J. Mech. Phys. Solids* **39,** 989–1015.

O'Dowd, N. P. and Shih, C. F. (1992). Family of crack-tip fields characterized by a triaxiality parameter—II. Fracture applications. *J. Mech. Phys. Solids* **40,** 939–963.

Parks, D. M. (1974). A stiffness derivative finite element technique for determination of crack tip stress intensity factors. *Int. J. Fracture* **10,** 487–501.

Rice, J. R. (1968). A path independent integral and the approximate analysis of strain concentration by notches and cracks. *J. Appl. Mech.* **35,** 379–386.

Rice, J. R. (1972). The line spring model for surface flaws. In *The Surface Crack: Physical problems and computational solutions* (Edited by J. L. Swedlow), pp. 171–185. The American Society of Mechanical Engineers, New York.

Shih, C. F., Moran, B. and Nakamura, T. (1986). Energy release rate along a three-dimensional crack front in a thermally stressed body. *Int. J. Fracture* **30,** 79–102.

Shih, C. F. and German, M. D. (1981). Requirements for a one parameter characterization of crack tip fields by the HRR singularity. *Int. J. Fracture* **17,** 27–43.

Shivakumar, K. N. and Newman, J. C., Jr (1992). Verification of effective thickness for side-grooved compact specimens. *Engng Fract. Mech.* **43,** 269–275.

Slepyan, L. I. (1974). Growing cracks during plane deformation of an elastic-plastic body. *Izv. Akad. Nauk SSSR. Mekhanika Tverdogo Tela.* **9,** 57–67 (Translated from Russian).

Sönnerlind, H. and Kaiser, S. (1986). The *J*-integral for a SEN specimen under nonproportionally applied bending and tension. *Engng Fract. Mech.* **24,** 637–646.

Williams, M. L. (1957). On the stress distribution at the base of a stationary crack. *J. Appl. Mech.* **24,** 109–114.